JOURNAL OF SPACECRAFT AND ROCKETS
Vol. 39, No. 3, May–June 2002

Numerical Investigation of Supersonic Jet Interaction for Finned Bodies

Mary Jane Graham*
U.S. Military Academy, West Point, New York 10996-1786
Paul Weinacht†
U.S. Army Research Laboratory, Aberdeen Proving Ground, Maryland 21005-5066
and
Julius Brandeis‡
RAFAEL, Ministry of Defense, 31021 Haifa, Israel

A detailed numerical investigation of the interaction between a lateral jet and the external flow has been performed for a variety of missile body geometries. These include nonfinned axisymmetrical bodies and finned bodies with either strakes or aft-mounted tail fins. The computations were performed at Mach numbers 2 and 4.5. To obtain the numerical results, both thin layer Reynolds-averaged Navier–Stokes and Euler techniques were applied. The computational results were compared with results from a previously published wind-tunnel study that consisted primarily of global force and moment measurements. The numerical techniques showed good agreement with the experiments at supersonic Mach numbers. For the results examined here, there were only minor differences in the global force and moment predictions when viscous or inviscid techniques were used. The dependence of the interaction parameters on angle of attack and jet pressure were well predicted by both methods. The computational investigation also provided additional understanding of the wind-tunnel results. The computational results show significant interactions of the jet-induced flowfield with the fin surfaces that produce additional effects compared with the body alone. The computational and experimental results indicate deamplification of the jet force at Mach 2 for all three bodies. At Mach 4.5, amplification of the jet force was found, except for negative angles of attack for the bodies with less surface area than the straked case.

Nomenclature

a_∞	=	freestream speed of sound
$C_{m_{\text{jet-off}}}$	=	jet interaction moment coefficient without jet, normalized by $\frac{1}{2}\rho_\infty a_\infty^2 M_\infty^2 S_{\text{ref}} D$
$C_{m_{\text{jet-on}}}$	=	jet interaction moment coefficient with jet, normalized by $\frac{1}{2}\rho_\infty a_\infty^2 M_\infty^2 S_{\text{ref}} D$
C_{N_j}	=	jet force coefficient, normalized by $\frac{1}{2}\rho_\infty a_\infty^2 M_\infty^2 S_{\text{ref}}$
$C_{N_{\text{ji}}}$	=	jet interaction force coefficient, normalized by $\frac{1}{2}\rho_\infty a_\infty^2 M_\infty^2 S_{\text{ref}}$
D	=	projectile diameter
$\hat{\boldsymbol{E}}, \hat{\boldsymbol{F}}, \hat{\boldsymbol{G}}$	=	flux vectors in transformed coordinates
e	=	total energy per unit volume
F_j	=	force produced by the lateral jet
F_{ji}	=	force produced by jet interaction with external flow
$F_{\text{no-jet}}$	=	force produced in the absence of the jet
K	=	jet interaction amplification factor
M_∞	=	freestream Mach number
P_{oj}	=	jet stagnation pressure
p	=	pressure
q	=	dependent variables, $[\rho, \rho u, \rho v, \rho w, e]^T$
Re	=	Reynolds number, $a_\infty \rho_\infty D/\mu_\infty$
S_{ref}	=	reference area of projectile, $\pi D^2/4$
$\hat{\boldsymbol{S}}$	=	viscous flux vector
t	=	time
u, v, w	=	velocity components in x, y, and z directions
X_{cp}	=	interaction center of pressure location
x, y, z	=	axial, horizontal, and vertical coordinates
α	=	angle of attack
γ	=	ratio of specific heats
ΔC_m	=	jet interaction moment coefficient, normalized by $\frac{1}{2}\rho_\infty a_\infty^2 M_\infty^2 S_{\text{ref}} D$
μ	=	viscosity
ξ, η, ζ	=	transformed coordinates in Navier–Stokes equations
ρ	=	density

Subscript

∞	=	freestream conditions

Introduction

THE flowfield that results from the interaction of a side (lateral) jet injection into a supersonic external flow, called the jet interaction flowfield, has been the subject of several experimental[1–5] and numerical[6–11] investigations. The typical jet interaction flowfield is complicated because of the jet's interruption of the oncoming external flow. The qualitative features of the jet interaction flowfield include regions of shock–boundary-layer interaction and flow separation that have an effect on the overall flow around the body. In previous work,[11] a detailed numerical study was performed for finless axisymmetrical bodies. In this paper, results are presented for missiles with several fin–body geometries that incorporate body strakes and aft-mounted fins. It was shown previously[11] that for a finless body, a decrease in the force amplification factor occurred partially because the jet bow shock wrapped around and interacted with the flow underneath the body. The presence of strakes has the effect of blocking the wrap-around phenomena and channeling the high-pressure flow down the body, therefore allowing for amplification. The purpose of the current research is to develop a reliable computational capability to assess the performance of control jets and to obtain a quantitative understanding of the flow phenomenon produced by control jets in the presence of strakes and/or

Received 16 August 2001; revision received 6 December 2001; accepted for publication 7 December 2001. This material is declared a work of the U.S. Government and is not subject to copyright protection in the United States. Copies of this paper may be made for personal or internal use, on condition that the copier pay the $10.00 per-copy fee to the Copyright Clearance Center, Inc., 222 Rosewood Drive, Danvers, MA 01923; include the code 0022-4650/02 $10.00 in correspondence with the CCC.

*Assistant Professor, Department of Mathematical Sciences. Member AIAA.

†Aerospace Engineer, Weapons and Materials Research Directorate, Ballistics and Weapons Concepts Division. Associate Fellow AIAA.

‡Senior Research Engineer, Aeronautical Systems Department, Missile Division. Member AIAA.

fins at supersonic Mach numbers and to demonstrate that computational fluid dynamics (CFD) simulation is capable of predicting the important features of jet interaction phenomenon.

This paper primarily addresses viscous techniques, but we have also examined the ability to use, and the feasibility of using, inviscid techniques to predict the same flowfields. Numerical predictions of the supersonic viscous flow have been obtained with a Reynolds-averaged Navier–Stokes solver and Euler techniques. Comparisons between viscous and inviscid results can shed new light on the significance of viscous effects (i.e., separation of flow because of shock interaction) in overall vehicle forces and moments.

In addition to the use of several different geometries, the parameters that were varied in this study are Mach number, angle of attack, and jet stagnation pressure. The parameters in the computational study are those used in the experimental work of Brandeis and Gill.[5] The experimental Mach numbers are 2.0 and 4.5, and the angles of attack range from −10 to 10 deg. The jet stagnation pressure varies from 3.6 to 72 atm. It will be shown that the numerical results collaborate the experimental findings, in which the presence of strakes caused large control force amplification. The amplified control force associated with the strakes permits the use of smaller control jets and, therefore, results in propellant volume and weight savings.

In the present study, numerical approaches have been applied to investigate the jet interaction phenomena for flight bodies with lifting surfaces with a single lateral jet in supersonic flight and to demonstrate the advantages to force amplification factor in the presence of these surfaces. An overset grid approach has been applied to resolve more easily the geometry and flow physics associated with the jet interaction problem. All of the numerical results have been validated via global force and moment data from a recently published experimental investigation.[5]

Computational Technique

Governing Equations

The nonreacting compressible viscous flow, which obeys the Newtonian law of friction about a flight vehicle, is governed by the equations of mass, momentum, and energy conservation: the Navier–Stokes equations. For these computations, the complete set of three-dimensional, time-dependent, generalized-geometry, Reynolds-averaged, thin-layer Navier–Stokes equations for generalized coordinates ξ, η, and ζ are used and can be written as follows[12]:

$$\frac{\partial \hat{q}}{\partial t} + \frac{\partial \hat{\boldsymbol{E}}}{\partial \xi} + \frac{\partial \hat{\boldsymbol{F}}}{\partial \eta} + \frac{\partial \hat{\boldsymbol{G}}}{\partial \zeta} = \frac{1}{Re}\frac{\partial \hat{\boldsymbol{S}}}{\partial \zeta} \tag{1}$$

where $\xi = \xi(x, y, z, t)$, $\eta = \eta(x, y, z, t)$, and $\zeta = \zeta(x, y, z, t)$ are the longitudinal coordinate (direction along the body), the circumferential coordinate (direction around the body), and the nearly normal coordinate (outward direction from the body surface), respectively.

The local pressure is related to the dependent variables by applying the ideal gas law:

$$p = (\gamma - 1)[e - 0.5\rho(u^2 + v^2 + w^2)] \tag{2}$$

in which γ is the ratio of specific heats. Density ρ is normalized by ρ_∞; the velocities u, v, and w by a_∞; and the total energy e by $\rho_\infty a_\infty^2$.

The form of the mass-averaged Navier–Stokes equations requires a model for the turbulent eddy viscosity. There are numerous approaches for determining the turbulent viscosity. The turbulent contributions are supplied through the algebraic two-layer eddy viscosity model developed by Baldwin and Lomax,[13] which is patterned after the model of Cebeci.[14]

Navier–Stokes Numerical Technique

The time-dependent Navier–Stokes equations are solved using a time-iterative solution technique to obtain the final steady-state converged solution. The particular time-marching technique applied here is the implicit, partially flux-split, upwind numerical scheme developed by Ying et al.[15] and Sahu and Steger[16] and is based on the flux-splitting approach of Steger and Warming.[17] This scheme employs central differencing in the normal and circumferential directions, η and ζ, respectively, and flux splitting in the streamwise direction ξ.

Chimera Composite Overset Structured Grids

To model more easily, the geometry and resolve the flow physics associated with the lateral jet problem, the chimera composite overset grid technique[18–20] has been applied. The chimera technique is a domain decomposition approach that allows the entire flowfield to be meshed into a collection of independent grids, where each piece is gridded separately and overset into a main grid. In current computations, the flight body with lateral jet was subdivided into three distinct grids: one for the body, one adjacent to the jet, and one for the jet nozzle. Overset grids are not required to join in any special way. Usually, there is a major grid that covers the main domain (the external flowfield about the projectile), and minor grids are generated to resolve the rest of the body or sections of the body (the jet and the nozzle regions).

Figure 1 displays the computational mesh, showing the main grid for the projectile body along with an overset grid to capture better the physics of the jet interaction with the external flow. The overset jet grid is seen here residing on top of the jet exit as a cylinder with a radius larger than the jet nozzle opening itself. A third grid, used to model the jet nozzle, resides underneath the jet grid. The communication between the nozzle grid and the jet grid, however, is point-to-point zonal. Figure 2 is a close-up of the grid near the jet port, which is covered by the nozzle grid and jet grid. It also shows the chimera grid for the jet and the projectile body.

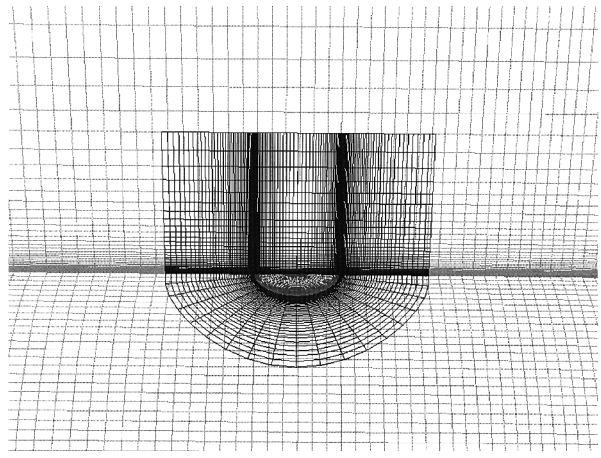

Fig. 1 Computational mesh.

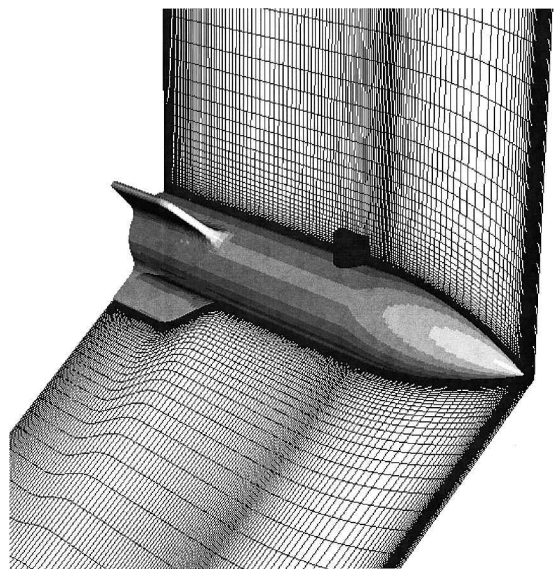

Fig. 2 Chimera gridding near jet nozzle.

Grid Refinement and Computational Time

The baseline computational grid used to generate the published results consisted of approximately 1.6 million points: $153 \times 93 \times 70$ for the projectile (background) grid in the longitudinal, circumferential, and normal directions, respectively; $65 \times 21 \times 50$ for the cylindrically shaped jet grid in the radial, circumferential, and normal directions, respectively; and $25 \times 21 \times 21$ for the nozzle grid in the radial, circumferential, and normal directions. The computational mesh employed a mirror plane of symmetry in the circumferential direction. A grid refinement study was performed to assess grid convergence for the baseline computational grid. Coarse grid solutions were obtained using $115 \times 107 \times 58$, $49 \times 16 \times 38$, and $19 \times 16 \times 16$ grids for the projectile, jet, and nozzle meshes, respectively. Fine grid solutions were obtained using $189 \times 167 \times 84$, $78 \times 25 \times 60$, and $30 \times 25 \times 25$ grids for the projectile, jet, and nozzle meshes, respectively.

Comparisons were made of the forces, moments, amplification factor, and jet interaction center of pressure. Between the baseline computational grid and the finer grid, there is a 1.1% difference in the jet interaction force and a 1% difference in the moments, amplification factor, and the jet interaction center of pressure. For the coarser grid, there is a 1.2% difference in the jet interaction force, and a 1.1–2.0% difference in the moments, amplification factor, and the jet interaction center of pressure.

A complete simulation on the baseline grid took approximately 250 CPU h on an SGI Origin 2000. The solutions were run in parallel using eight processors, and a parallel speed-up of 5.4 was obtained.

Inviscid Technique

In addition to the earlier described Navier–Stokes approach, inviscid results were also obtained using the CFD code INCA.[21] INCA is a three-dimensional multiblock, Navier–Stokes solver with very general capabilities but is run in the Euler (inviscid) mode for the results presented in the current paper. These results were obtained independently of and before the results obtained with the earlier described Navier–Stokes code. Sophisticated memory management routines allocate space for zones and additional transport equations for chemical species and the turbulence quantities only as needed. A wide range of inflow, outflow, and wall boundary conditions are available to model complex three-dimensional flowfields. The field equations are solved using a lower–upper symmetric Gauss–Seidel (LU-SGS) implicit finite volume method. This type of algorithm has proven to be a robust and efficient relaxation procedure for steady-state flowfields. The evaluation of the inviscid terms is based on flux splitting in combination with upwind biasing. The INCA code currently supports two flux functions: the flux-vector splitting of Steger and Warming[17] and the symmetric total variational diminishing fluxes of Yee. The difference terms are evaluated using standard central differences. The LU-SGS algorithm is used to solve approximately the system of equations using two sweeps of a point Gauss–Seidel relaxation.

The numerical solution was run until convergence was reached. The degree of convergence of the solution was judged from the maximum field residue occurring at each time step for each block. In general, convergence level is different in each block, especially for cases with jet activation. Convergence level is indicated by the logarithm of the largest residual (rms, averaged for the field variables). Typically, the residuals were reduced by at least 10 orders of magnitude for results presented here. For the configuration without the jet, at Mach 4.5, convergence to the level where the maximum residual of 10^{-13} in each of the four blocks was obtained in fewer than 1000 iterations. For a typical jet-on case, convergence to levels better than 10^{-8} is achieved within 1000 cycles. From the point of view of integral parameters, such as forces and moments obtained from pressure integration, there is no variation after the residual decreased three or four orders of magnitude.

Computational Grid Generation

The grid is divided into four blocks, which is the minimum number of blocks needed to cover the given topology. One grid block was used on the axisymmetrical nose and the remaining three grids were arranged circumferentially on the finned portion of the body. Two grid blocks were placed between the half-plane of symmetry and an adjacent fin, and the remaining grid block was placed between the two fins to form the middle of the domain. Use is made of the commercially available, general purpose, three-dimensional, multiblock structured grid generator using an advanced smoothing scheme called GridPro.[22] The final grid topology used in the inviscid computation of the flowfield over the configuration without the jet has about 70,000 grid points. The jet nozzle has a diameter of 0.5 cm, which is comparable in size to one finite difference cell. To obtain better resolution, local grid refinement in the vicinity of the jet nozzle was performed offline, and the number of grid points defining the nozzle has been quadrupled. Away from the body surface, the grid becomes coarser. Although the coarse grid away from the jet area will affect the definition of shocks (the shocks are formed of several grid points, which, when far apart, will give a smeared and wavy appearance), the solution close to the body surface will not be affected in the supersonic calculations. The refined grid, giving good definition of the nozzle size and location, consists of about 120,000 points. The block structure described earlier is retained.

Grid Refinement Study (Grid Independence)

For the configuration presented here, the jet-off case (inviscid) was computed with and without the local grid refinement performed to resolve better the area containing the nozzle and the wings' leading edges (120,000 points vs 70,000 points). No difference in solution was observed within plotting accuracy. Grid sensitivity analyses were performed for a prototype configuration, different from the present configuration only in some dimensions. For that configuration (not presented), several grids were used, the finest being coarser than the unrefined grid used in the present report. The graphical results for two successive grids were indistinguishable.

Results

The results from the computational approach for the jet interaction problem were compared with data from a previously published wind-tunnel investigation.[5] Supplemental experimental results for the validation were provided courtesy of RAFAEL, Ministry of Defense, Missiles Division, Aeronautical Systems Department. The experiments were conducted at the Israel Aircraft Industries trisonic wind-tunnel facility at Mach numbers of 2 and 4.5. Although the experimental investigation was quite extensive in scope, the current computational study focused on normal jet injection from a single nozzle geometry at Mach 2 and 4.5. Five different configurations were examined in the experimental study; three cases are examined in this paper. Global force and moment comparisons were made to validate the computational approach for Mach numbers 2 and 4.5.

Figure 3 shows three body geometries addressed in this study. Each of the models used has a sharp, tangent ogive-shaped nose section of 2.5 calibers and a cylindrical afterbody of 3.8 calibers mounted on the midsection for a total length of 5.8 calibers. The reference diameter of the models was 50 mm. For all three geometries, the jet nozzle was located 2.5 calibers downstream from the nose tip. A single circular nozzle of 0.1 calibers that was designed to achieve sonic flow at the exit was examined here, although additional geometries were considered in the experiment. The strake and

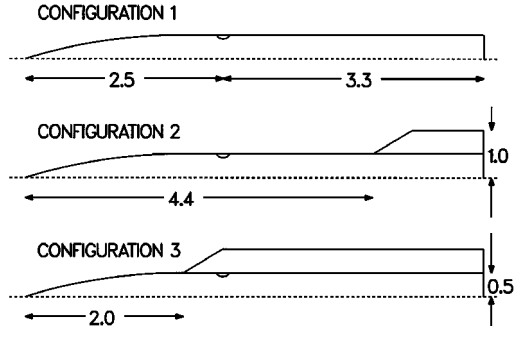

Fig. 3 Schematic of body geometries; dimensions in calibers.

aft-mounted fins (of which there are four, equally spaced) have the same exposed semispan of 0.5 calibers and the leading-edge sweep angle of 45 deg. Relative to the jet, the fins and strakes are located 45 deg (roll position); elsewhere, the lifting surfaces are separated by 90 deg. Configuration 1 is an axisymmetrical body-alone configuration used as a reference configuration for comparison. Configuration 2 has an aft-mounted tail fin. The root leading edge of each tail surface is located 4.4 calibers from the nose tip. Configuration 3 contains strakes spanning 65% of the body's length. The root leading edge is two calibers from the nose tip.

For the jet interaction problem, the total force acting on the body can be decomposed into three components: the aerodynamic force on the external body in the absence of the jet, the force produced solely by the jet, and the aerodynamic interaction force produced by the jet with the external flowfield. In this work, the aerodynamic force on the external body is typically produced when the body is at an angle of attack with the freestream flow. The force produced at the jet exit results from a combination of the momentum flux through the jet nozzle and the integrated pressure at the jet exit. Given that the exit conditions for the jet are fixed as a boundary condition for the computations, this force component can be explicitly calculated before the flowfield computation. The third force component accounts for the force produced by the interaction of the jet with the external flowfield.

The relationship of these three force components to the total force F can be described by the following equation, where $F_{\text{no-jet}}$ is the force in the absence of the jet, F_j is the force produced at the jet exit, and F_{ji} is the jet interaction force:

$$F = F_{\text{no-jet}} - (F_j + F_{\text{ji}}) \tag{3}$$

The negative sign associated with the two jet forces results because the jet exit hole is located on the upper surface of the body in the current study and produces a downward force when activated. The jet-off force component typically produces an upward force for positive angles of attack. Note that a positive value of F_{ji} indicates that the interaction force produces an effect that augments the jet force F_j, whereas a negative value of F_{ji} indicates a reduction in the total force produced by the jet. The jet interaction force accounts for the complete interaction produced by the jet with the external flowfield and may vary with angle of attack and jet mass flow rate.

The relative magnitudes of the jet force and the jet interaction force can be compared through a jet interaction amplification factor K, as shown in Eq. (4):

$$K = (F_j + F_{\text{ji}})/F_j \tag{4}$$

An amplification factor greater than one indicates that the jet interaction force amplifies or increases the total force produced by the jet, whereas an amplification factor less than one indicates that the jet interaction force reduces the total force produced by the jet.

In addition to the jet interaction forces, the interaction moments were calculated. In the present case, the center of moments is taken to be the center of the jet nozzle, the assumed center of gravity. The moments considered are pure interaction moment effects calculated as follows:

$$\Delta C_m = C_{m_{\text{jet-on}}} - C_{m_{\text{jet-off}}} \tag{5}$$

in which $C_{m_{\text{jet-on}}}$ is the moment coefficient for the configuration with the jet and $C_{m_{\text{jet-off}}}$ is the moment coefficient for the configuration without the jet.

The moment interaction can also be assessed by examining the jet interaction center of pressure, which defines the axial location where the net jet forces (both jet thrust and jet interaction force) act relative to the jet nozzle location. The jet interaction center of pressure in calibers is defined as follows, with a positive jet interaction center of pressure indicating a rearward location, or, correspondingly, a nose-down pitching moment for a positive jet force:

$$X_{\text{cp}} = \frac{-\Delta C_m}{C_{N_j} + C_{N_{\text{ji}}}} \tag{6}$$

Figures 4 and 5 display the variation of the force amplification factor with angle of attack at Mach 2 and 4.5 for the body alone and body with tail fins. This particular body comparison is meaningful because in front of the tail fins (for these supersonic flow cases), the force amplification is essentially identical for both bodies. The differences in the force amplification factor for these two bodies occur only over the aft 1.4 calibers of the body where the fins are located. The predicted results for the force amplification factor show excellent agreement with experiment between −10- and 10-deg angle of attack.

An increasing trend in the force amplification factor is noted with increasing Mach number in Figs. 4 and 5 with deamplification observed at Mach 2 for all Mach numbers and a mix of deamplification and amplification at Mach 4.5, depending on angle of attack. Although these three cases do not indicate a purely Mach number effect because the jet conditions are not identical or scaled, the results do appear to represent a general trend with Mach number. The CFD results indicate that the behavior of the jet interaction force and the jet amplification factor is influenced by two distinct regions in the flowfield. One of them is in the interaction region in front of the jet, where there is an area of high pressure behind the separation shock/wedge and jet bow shock. (See Fig. 6 overview of the vehicle

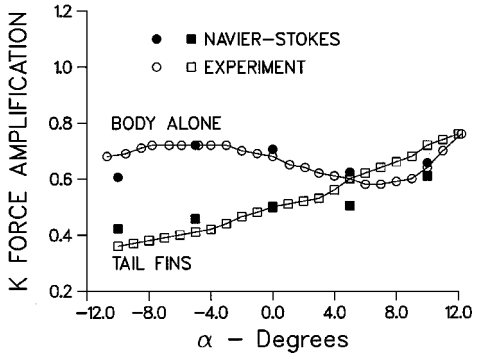

Fig. 4 Force amplification factor vs angle of attack; Mach 2, P_{oj} = 27 atm, body alone and tail fins.

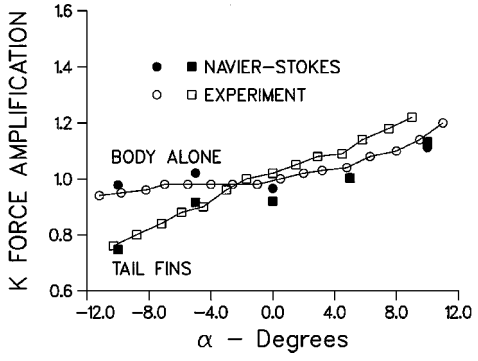

Fig. 5 Force amplification factor vs angle of attack; Mach 4.5, P_{oj} = 38 atm, body alone and tail fins.

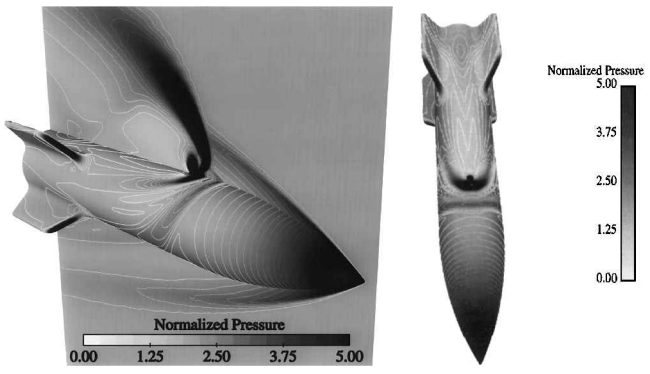

Fig. 6 Normalized pressure flowfield for the tail-finned body; Mach 2, α = 0 deg.

body.) This high-pressure region results in an interaction force that augments the jet thrust. The other area of influence is downstream of the jet, where there is a low-pressure region due to the jet blockage and entrainment. The force produced in the low-pressure region opposes the jet thrust and produces deamplification.

The presence of the jet causes a complex jet interaction flowfield as shown in Fig. 6. When the jet is on, it produces a blockage to the oncoming flow directly upstream of the jet. The jet acts as an obstacle to the external flow, causing a shock wave to originate (jet bow shock) and causing a boundary-layer separation region to form. The jet bow shock is seen in the side view of the vehicle down in Fig. 6, as well as the separation region, which is the ramp shaped region seen upstream of the jet bow shock. The jet bow shock bends backward, being deflected by the external flow, and moves laterally around the flight vehicle. The strong turbulent wake caused by the jet interaction flowfield interactions extends over a significant portion of the flight vehicle. Directly behind (downstream) of the jet emission, a vacuumlike region of low pressure is formed.

The relative effect of the regions described on the computed jet interaction force is shown in Figs. 7 and 8, where the development of the jet interaction force over the body is calculated for the body alone and tail fin geometries at $\alpha = \pm 10$ deg. The amplification of the jet interaction force in front of the jet due to the high-pressure region is apparent, and the effect of the low-pressure, vacuumlike region is strongly felt downstream of the jet. It is seen that the magnitude of the amplification is not as large in Fig. 8 as in Fig. 7. Although the local static pressure ratio in front of the jet increases with increasing Mach number, the force coefficient decreases with increasing Mach number because the rate of pressure increase is less than the Mach number squared. (The force coefficient is normalized by the Mach number squared.)

The deamplification produced by the low-pressure region behind the jet is also apparent in Figs. 7 and 8. Unlike the high-pressure region where the pressure can rise to many multiples of the freestream static pressure as the Mach number increases, the pressure behind the jet can go no lower than vacuum. The result is that if the similar levels of low pressure exist as the Mach number increases, the force coefficient produced by these pressures has much less of an effect because the force coefficient is normalized by the Mach number squared.

At Mach 2, deamplification of the jet interaction force for the entire body occurs because the low-pressure region behind the jet produces a larger effect than the high pressure in front of the jet. As the Mach number increases, the low-pressure region behind the jet has less of an effect, and the force amplification factor increases as the Mach number increases.

The variation of the force amplification factor with angle of attack is also influenced by the relative effect of the high- and low-pressure regions. The high-pressure region in front of the jet does show a modest decrease as the angle of attack changes from negative to positive angles of attack. This variation is due to the shadowing effect induced by the body on the lee side (jet side) at positive angles of attack. However, the dominant angle of attack effect is produced in the low-pressure region behind the jet. In the absence of the jet, the body experiences high pressure on the windward side and lower pressure on the leeward side. When the jet is on the windward side (negative angles of attack), a larger drop in pressure is possible between the jet-off and jet-on conditions than when the jet is on the leeward side because the pressure in the low-pressure region cannot drop below vacuum.

As indicated by the results, the presence of tail fins can result in further variations in the force amplification factor. For these supersonic results, the high-pressure region in front of the jet and the low-pressure region behind the jet are virtually unaffected by the presence of the tail fins. The implication is that the variations in the force amplification factor produced by the presence of the tail fins is a separate effect that occurs in addition to the effects observed for the body alone. The largest differences in the force amplification factor occur at negative angles of attack. The CFD results indicate that a significant portion of the jet-off fin lift is produced by windward fins and the cylinder between the windward fins. For negative incidences, the tail fins, particularly the windward fins, are immersed in the wake from the jet, which reduces the effectiveness of the fins relative to the jet-off case. At positive angles of attack, the jet wake flows away from the body, and the flowfield at the fins more closely resembles the jet-off case.

Figures 9 and 10 display the variation of the force amplification factor with angle of attack at Mach 2 and 4.5 for the straked body. The results are in good agreement with the experimental data across the range of angles of attack. At Mach 4.5 results were obtained with an inviscid code, as well as with the Navier–Stokes code. There is very little difference in the predicted results with either code. The similarity between the predicted results is significant, considering that the results were obtained independently with different codes and computational grids.

The general trend of increasing amplification factor with increasing Mach number, observed for the body alone and body with tail fins cases, is also present for the body with strakes. Flow visualization studies using the CFD results indicate that the jet interaction effect is, for the most part, confined to the region between the strakes adjacent to the jet nozzle. The increased restriction of the flow between the strakes can be easily seen in the overhead view of the

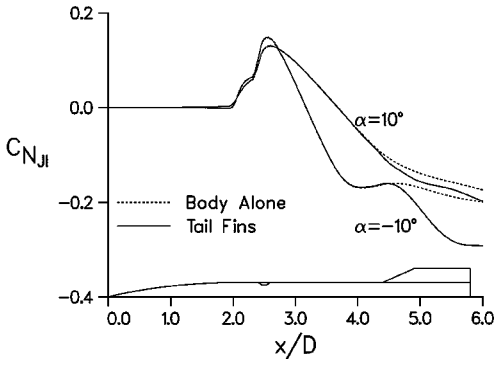

Fig. 7 Distribution of the computed jet interaction force over body; Mach 2, P_{oj} = 27 atm, body alone and tail fins, $\alpha = \pm 10$ deg.

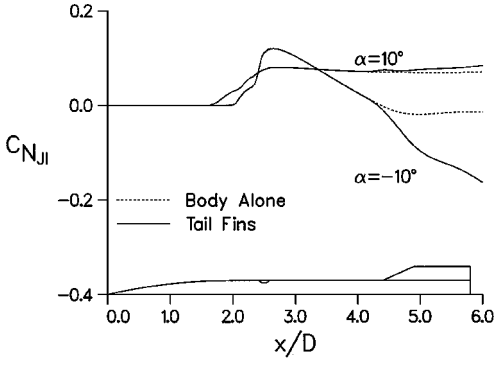

Fig. 8 Distribution of the computed jet interaction force over body; Mach 4.5, P_{oj} = 38 atm, body alone and tail fins, $\alpha = \pm 10$ deg.

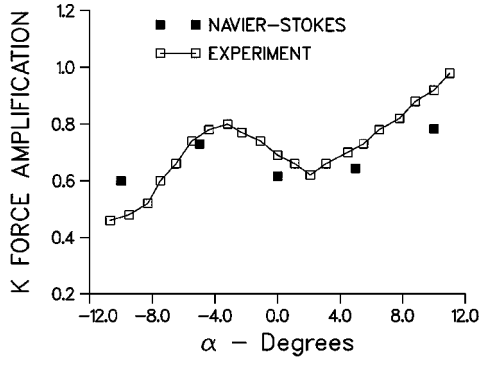

Fig. 9 Force amplification factor vs angle of attack; Mach 2, P_{oj} = 27 atm, strakes.

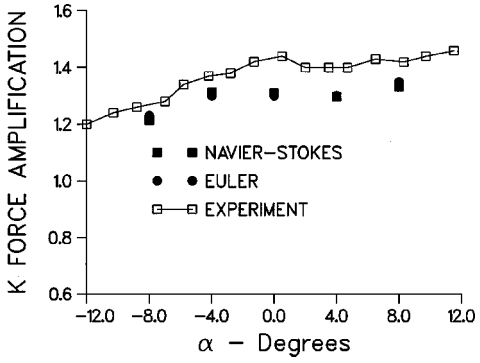

Fig. 10 Force amplification factor vs angle of attack; Mach 4.5, $P_{oj} = 38$ atm, strakes.

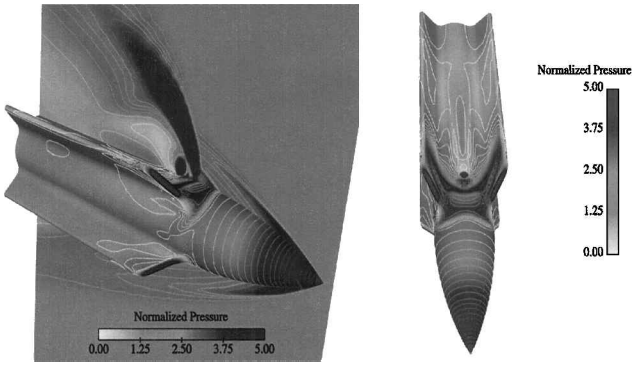

Fig. 11 Normalized pressure flowfield for the straked body; Mach 2, $\alpha = 0$ deg.

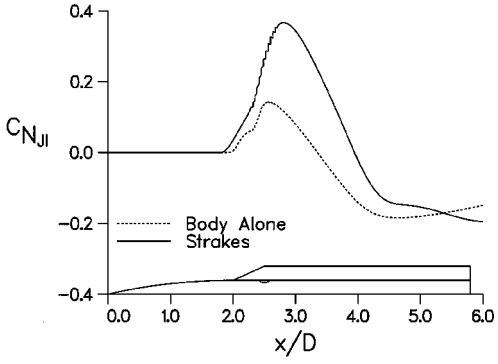

Fig. 12 Distribution of the computed jet interaction force over body; Mach 2, $P_{oj} = 27$ atm, body alone and straked body, $\alpha = 0$ deg.

flight vehicle in Fig. 11 (the log normal of the pressure, for the Mach 4.5 case at zero angle of attack). In the straked case, the jet bow shock is bent backward by the oncoming external flow; however, the lateral movement of the jet bow shock is blocked by the strakes. Like the body-alone and tail fin configurations, there exists a high-pressure region produced by the jet bow shock in front of the jet and a low-pressure region behind the jet. For the straked configurations, the high- and low-pressure regions act not only on the cylindrical body but also on the adjacent strake surfaces. The additional surface area upon which these pressures act can amplify the effects observed earlier for the body alone cases. A comparison of the distribution of the jet interaction force over the bodies points out the differences. As shown in Fig. 12, at Mach 2, the high-pressure region for the straked body produces nearly twice the amplification as for the body-alone/tail fin case (Fig. 7). The low-pressure region also produces a larger deamplification effect as well. Similar behavior is also seen at Mach 4.5.

Calculations were performed for jet stagnation pressure ranging from 3.6 to 72 atm. Figure 13 shows the variation of the force amplification factor with jet pressure at 0-deg angle of attack for Mach

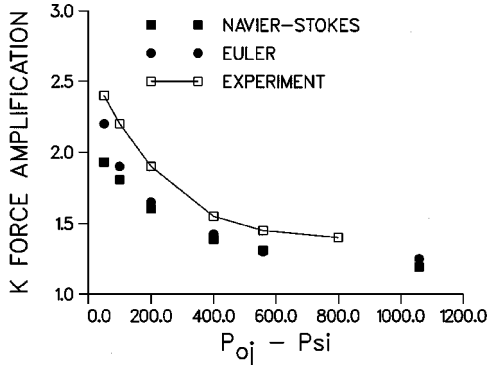

Fig. 13 Force amplification factor as a function of jet pressure; Mach 4.5, $\alpha = 0$ deg, straked body.

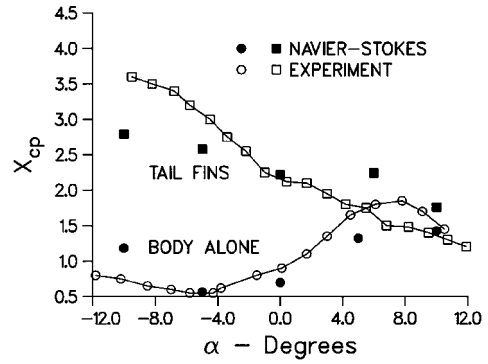

Fig. 14 Center of pressure vs angle of attack; Mach 2, $P_{oj} = 27$ atm, body alone and tail fins.

4.5 for both Navier–Stokes and Euler calculations. It is found that the force amplification factor decreases with increasing jet pressure because the force due to the jet increases faster than the jet interaction force. Note that the jet force is directly related to the jet pressure and increases nearly linearly with increasing jet pressure. Although the size of the interaction region and the magnitude of the jet interaction force increase with increasing jet pressure, the rate of the increase is not as large as the corresponding change in the jet force. The sharp decreasing trend in force amplification as jet pressure increases is captured by both the inviscid and viscous simulations. The predicted force amplification factor as a function of jet pressure exhibits the same quantitative variation as the experiment, slightly underpredicting the magnitude.

It was originally anticipated that a viscous code would close the gap between the Euler prediction and experimental results. The computational results suggest that the differences are not due to viscous effects. It is believed that the discrepancy is strongly related to the difference between the measured and calculated values of the net jet thrust, even though the measured net jet thrust was corrected for various factors. The final experimental value of F_j used in calculating K was 20% less than the computed value. Therefore, the underprediction of K by the computations arises partly because of the idealized calculation of the net jet thrust at low injection pressures.

Figures 14–17 show the jet interaction center of pressure as a function of angle of attack at Mach 2 and 4.5 for each of the three bodies. In general, the predicted variation of X_{cp} with angle of attack is in good agreement with the experimental data. X_{cp} defines the location where the net jet force acts. X_{cp} is predominantly a positive number. Positive X_{cp} indicates a nose-down pitching moment and a center of pressure location to the rear of the jet nozzle. At Mach 2, X_{cp} is located further aft than at the higher Mach numbers due to the influence of the low-pressure region behind the jet. As the Mach number increases and the influence of the low-pressure region decreases, X_{cp} moves forward toward the jet nozzle. As noted earlier for the force amplification factor at higher positive angles of attack, the tail fin and body-alone results are similar because there is little influence of the jet wake on the tail fins. As the angle of attack

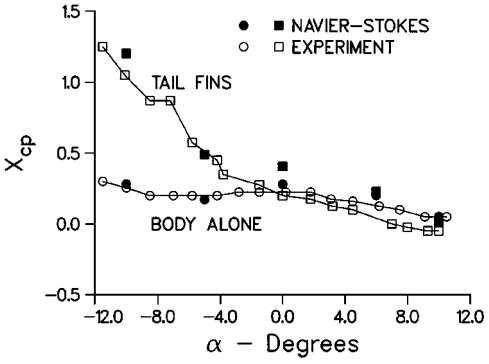

Fig. 15 Center of pressure vs angle of attack; Mach 4.5, P_{oj} = 38 atm, body alone and tail fins.

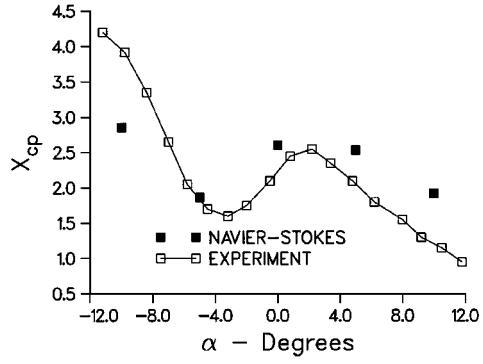

Fig. 16 Center of pressure vs angle of attack; Mach 2, P_{oj} = 27 atm, straked body.

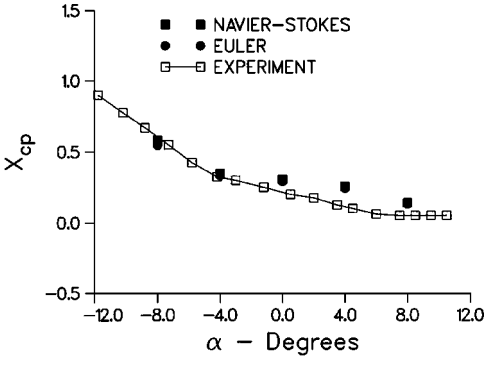

Fig. 17 Center of pressure vs angle of attack; Mach 4.5, P_{oj} = 38 atm, straked body.

decreases, the influence of the wake on the tail fins increases, producing a rear movement in the center of pressure. For the straked body, decreased variations of X_{cp} were observed with increasing Mach number, as well as a rearward movement in X_{cp} at negative angles of attack. Also shown in Fig. 17 is a comparison of the prediction of the jet interaction center of pressure using the Navier–Stokes and Euler techniques at Mach 4.5. The Navier–Stokes and inviscid predictions are essentially equivalent and agree well with the experimental data. Similar agreement was shown earlier for the force amplification factor.

Conclusions

A computational study has been conducted to examine the jet interaction effect for a finless axisymmetric body and two finned configurations in supersonic flight at various Mach numbers, angles of attack, and for, various jet injection pressures. The finned bodies include a body with aft-mounted tail fins and a body with lifting strakes. The predictions were compared with data from a previously published wind-tunnel investigation to validate the predictive capability. Good agreement is found at Mach 2 and 4.5, and the variation of the jet interaction forces and moments with Mach number, angle of attack, and jet injection pressure is well predicted.

The results show significant interactions of the jet-induced flowfield with the fin surfaces that produce additional effects compared with the body alone. The CFD results indicated that for the body-alone case, there were two important interaction regions, the high-pressure region in front of the jet and the low-pressure region behind the jet. The high-pressure region was evident for all Mach numbers examined. The low-pressure region had its largest effect at Mach 2, where it resulted in a deamplification of the jet interaction force for the body. As the Mach number increased, the low-pressure region played a less important role in the jet interaction force and moment. The body with tail fins exhibited an additional jet interaction effect due to the interference of the jet wake with the tail fins. This effect was most evident at negative angles of attack where the jet wake interacts most strongly with the tail fins. At larger positive angles of attack, there was little interaction between the jet wake and the fins, and the resulting interaction was similar to the body alone case.

For the straked body, a strong interaction between the jet-induced flowfield and the lifting surfaces was observed. The interaction region was confined to the area between the lifting surfaces adjacent to the jet nozzle. The CFD results revealed that the high- and low-pressure regions observed for the body-alone case were also present for the straked body. However, the strakes provided additional surface area for these pressures to act. This resulted in larger interaction forces from the high-pressure region compared with body alone, although, at Mach 2, the interaction force from the low-pressure region was large enough to produce a significant force deamplification for the complete configuration.

The results show deamplification of the jet force at Mach 2 for all three bodies and a mix of deamplification and amplification for Mach 4.5 depending on angle of attack. Generally, amplification factors increased somewhat with increasing angle of attack for all three bodies.

For the results examined here, there were only minor differences in the transverse global force and moment predictions using viscous or inviscid techniques. Of course, significant differences in the axial force due to viscous drag were apparent. The differences are not due to jet effects. The similarity between the Navier–Stokes and Euler solutions indicates that the importance of viscous effects on the jet interaction forces and moments is small for these configurations, especially in view of the large lifting surfaces that receive the pressure forces. Both techniques correctly predicted the dependence of the interaction parameters on angle of attack and jet pressure. The results indicate that, for the purpose of overall design of configurations with jet force control, the inviscid methods may be both sufficient and expedient. Viscous computations are, however, imperative when the near field close to the jet is considered.

Acknowledgments

The experimental data that formed the basis for the computational validation were provided courtesy of RAFAEL, Israel Ministry of Defense Directorate of Defense Research and Development. This work was supported, in part, by a grant of computer time from the U.S. Department of Defense High Performance Computing Modernization Program of the U.S. Army Research Laboratory Major Shared Resource Center, Aberdeen Proving Ground, Maryland. We would like to thank R. Angelini for his work on the scientific visualization of the computed flowfields. Angelini is from the Computing Technologies Branch, High Performance Computing Division, Computational and Information Sciences Directorate, of the U.S. Army Research Laboratory at Aberdeen Proving Ground, Maryland.

References

[1] Brandeis, J., and Gill, J., "Experimental Investigation of Side-Jet Steering for Supersonic and Hypersonic Missiles," *Journal of Spacecraft and Rockets*, Vol. 33, No. 3, 1996, pp. 346–352.

[2] Spaid, F. W., and Zukoski, E. E., "Study of the Interaction of Gaseous Jets from Transverse Slots with Supersonic External Flows," *AIAA Journal*, Vol. 6, No. 2, 1968, pp. 205–212.

[3] Gilman, R. G., "Control Jet Interaction Investigation," *Journal of Spacecraft and Rockets*, Vol. 8, No. 4, 1971, pp. 334–339.

[4]Spaid, F. W., "Two-Dimensional Jet Interaction Studies at Large Values of Reynolds and Mach Numbers," *AIAA Journal*, Vol. 13, No. 11, 1975, pp. 1430–1434.

[5]Brandeis, J., and Gill, J., "Experimental Investigation of Super- and Hypersonic Jet Interaction on Missile Configurations," *Journal of Spacecraft and Rockets*, Vol. 35, No. 3, 1998, pp. 296–302.

[6]McMaster, D. L., Shang, J. S., and Golbitz, W. C., "Supersonic, Transverse Jet from a Rotating Ogive Cylinder in a Hypersonic Flow," *Journal of Spacecraft and Rockets*, Vol. 26, No. 1, 1989, pp. 24–30.

[7]Chamberlain, R., "Calculation of Three-Dimensional Jet Interaction Flowfields," AIAA Paper 90-2099, July 1990.

[8]Hsieh, T., and Wardlaw, A. B., "Numerical Simulation of Cross Jets in Hypersonic Flow Over a Biconic Body," AIAA Paper 94-0165, Jan. 1994.

[9]Sahu, J., "Numerical Computations of Three-Dimensional Jet Interaction Flowfields," AIAA Paper 94-3521, Aug. 1994.

[10]Srivastava, B., "Aerodynamic Performance of Supersonic Missile Body- and Wing Tip-Mounted Lateral Jets," *Journal of Spacecraft and Rockets*, Vol. 35, No. 3, 1998, pp. 278–286.

[11]Graham, M. J., and Weinacht, P., "Numerical Investigation of Supersonic Jet Interaction for Axisymmetric Bodies," *Journal of Spacecraft and Rockets*, Vol. 37, No. 5, 2000, pp. 675–683.

[12]Pulliam, T. H., and Steger, J. L., "Implicit Finite Difference Simulations of Three-Dimensional Flow," *AIAA Journal*, Vol. 18, No. 2, 1982, pp. 159–167.

[13]Baldwin, B. S., and Lomax, H., "Thin Layer Approximation and Algebraic Model for Separated Turbulent Flows," AIAA Paper 78-257, Jan. 1978.

[14]Cebeci, T., "Calculation of Compressible Turbulent Boundary Layers with Heat and Mass Transfer," AIAA Paper 70-741, June–July 1970.

[15]Ying, S. X., Steger, J. L., Schiff, L. B., and Baganoff, D., "Numerical Simulation of Unsteady, Viscous, High-Angle-of-Attack Flows Using a Partially Flux-Split Algorithm," AIAA Paper 86-2179, Aug. 1986.

[16]Sahu, J., and Steger, J. L., "Numerical Simulation of Three-Dimensional Transonic Flows," *International Journal for Numerical Methods in Fluids*, Vol. 10, 1990, pp. 855–873.

[17]Steger, J. L., and Warming, R. F., "Flux Vector Splitting of the Inviscid Gasdynamic Equations with Application to Finite-Difference Methods," *Journal of Computational Physics*, Vol. 40, 1981, pp. 263–293.

[18]Steger, J. L., Dougherty, F. C., and Benek, J. A., "A Chimera Grid Scheme," *Advances in Grid Generation*, edited by K. N. Ghia and U. Ghia, FED-Vol. 5, American Society of Mechanical Engineers, Fairfield, NJ, 1983, pp. 59–69.

[19]Benek, J. A., Donegan, T. L., and Suhs, N. E., "Extended Chimera Grid Embedding Scheme with Application to Viscous Flows," AIAA Paper 87-1126, June 1987.

[20]Meakin, R. L., "Composite Overset Structured Grids," *CRC Handbook of Grid Generation*, edited by J. F. Thompson, B. K. Soni, and N. P. Weatherill, CRC Press, Boca Raton, FL, 1999, pp. 11-1–11-20.

[21]"INCA: 3D Multi-Zone Navier–Stokes Flow Analysis with Finite Rate Chemistry," *User's Manual*, Amtec Engineering, Inc., Bellevue, WA, Jan. 1992.

[22]"GridPro/az3000—User's Guide and Reference Manual," Program Development Corp., White Plains, NY, Aug. 1994.

R. M. Cummings
Associate Editor